Advanced Functional Materials

ADVANCED FUNCTIONAL MATERIALS
www.afm-journal.de

RESEARCH ARTICLE

Tri-$HfGeTe_4$: Hybrid Tri/Tetragonal 2D Layers with Strong Anisotropy for Self-Powered In-Sensor Multidimensional Computing

Fafa Wu[1] | Jiangdong Zhang[1] | Wanfu Shen[3] | Chunguang Hu[3] | Weina Zhao[2] | Peng Yu[1] | Taicheng An[2]

[1]State Key Laboratory of Optoelectronic Materials and Technologies, Nanotechnology Research Center, Guangzhou Key Laboratory of Flexible Electronic Materials and Wearable Devices, School of Materials Science and Engineering, Sun Yat-sen University, Guangzhou, P.R. China | [2]Guangdong Key Laboratory of Environmental Catalysis and Health Risk Control, Institute of Environmental Health and Pollution Control, School of Environmental Science and Engineering, Guangdong University of Technology, Guangzhou, P. R. China | [3]State Key Laboratory of Precision Measuring Technology and Instruments, Tianjin University, Tianjin, P. R. China

Correspondence: Weina Zhao (zhaowngd@gdut.edu.cn) | Peng Yu (yupeng9@mail.sysu.edu.cn)

Received: 19 November 2025 | **Revised:** 31 December 2025 | **Accepted:** 21 January 2026

Keywords: in-sensor computing | multidimensional perception | polarization-resolved | spectrum-selective

ABSTRACT

Multidimensional optical sensing is crucial for advanced visual systems to accurately identify targets in complex environments. Most current two-dimensional (2D) computational devices, however, only respond to light intensity. A key challenge is to develop novel 2D materials capable of simultaneous polarization-resolved and spectrum-selective detection under low-power operation. Herein, we demonstrate that tri-$HfGeTe_4$, a narrow-bandgap (0.6 eV) 2D semiconductor, enables zero-bias, spectrally selective, polarity-sensitive photodetection for self-powered in-sensor multidimensional computing. Especially, 2D tri-$HfGeTe_4$ features a novel low-symmetry puckered layered structure, uniquely composed of trigonal and tetragonal rings, with the trigonal motifs being reported for the first time in 2D materials. Significantly, such a unique structure gives rise to significant in-plane anisotropy, with ratios reaching 2.08 at 671 nm and 1.86 at 1064 nm. Notably, the dominant polarization orientations of visible light and near-infrared light are orthogonal to each other, which greatly facilitates dual-band information discrimination. In addition, driven by the photothermoelectric effect, 2D tri-$HfGeTe_4$ devices can efficiently modulate bipolar photocurrent for feature extraction without external power. More importantly, the 2D tri-$HfGeTe_4$ system achieves more accurate target recognition with a high Intersection over Union (IoU) of 91%. This work paves the way for compact, efficient multidimensional visual perception systems, supporting the development of robust in-sensor computing.

1 | Introduction

Light serves as an exceptionally rich carrier of multidimensional information, encompassing intensity distribution, spectral composition, and polarization state, which collectively encode and map the inherent features of visual scene objects [1, 2]. Effectively capturing these multidimensional optical signals not only enables deeper insight into complex scenes but also significantly enhances the accuracy of target recognition tasks, thereby strongly supporting a wide range of advanced applications, such as environmental remote sensing, biomedical imaging, and autonomous driving [3–6]. However, most conventional

Fafa Wu and Jiangdong Zhang contributed equally to this work.

optoelectronic devices are primarily focused on perceiving light intensity—typically within the visible range—while losing critical features from the spectrum and polarization. Notably, spectral sensing (e.g., visible and near-infrared) can reveal hidden information and enhance adaptability to complex environments [7–9], while polarization detection can reduce interference and improve image contrast [10–13]. To expand detectable optical dimensions, the traditional approach typically involves cascading discrete photodetectors and integrating external optical components such as polarization units and optical filters. While this strategy can partially incorporate multidimensional information, it inevitably leads to bulky systems, complex structures, and high costs [14, 15]. Moreover, due to the physical separation of sensing and computing units, such systems inherently introduce redundant sampling and transmission processes, leading to undesirably high latency and energy consumption [16, 17]. Given the current trend toward integrated and intelligent visual systems, it is therefore urgently necessary to develop computational optoelectronic devices capable of responsively interpreting multidimensional optical information and efficiently extracting target features directly at the data capture point.

Benefiting distinctively from their unique crystal structures and exceptional physical properties, two-dimensional (2D) materials have recently emerged as a highly promising platform for optoelectronic applications [18–21]. Notably, the optical bandgap of various 2D materials spans broadly from ultraviolet to terahertz wavelengths, thereby significantly expanding the detectable spectral range [22–24]. Furthermore, in-plane anisotropic 2D materials—characterized by puckered layers or asymmetrical polygons, such as BP [25], GeSe [26], $GeAs_2$ [27], GeP [28], and PdPSe [29]—intrinsically exhibit pronounced polarization sensitivity. More importantly, by employing tunable responsivities as the weights, such photodetectors can efficiently execute multiply-and-accumulate (MAC) operations, thereby enabling feature extraction directly at the data capture point [30–32]. Consequently, considerable efforts have been dedicated to advancing optoelectronic devices and integrating them with neural networks for intelligent processing tasks, including object recognition, image classification, and semantic segmentation [33–36]. However, current in-sensor computing devices predominantly rely on heterostructure integration to broaden detectable optical dimensions and on electrical gating to modulate photoresponse [6, 7, 9, 30, 34]—unfortunately, these approaches inevitably increase structural complexity and introduce additional power consumption. Thus, it remains highly challenging to integrate polarization sensitivity, spectral selectivity, and in-sensor computing within a single device without resorting to heterogeneous integration or external gate modulation.

Encouragingly, certain in-plane anisotropic materials can exhibit spectrally selective, polarization-sensitive behavior across different wavelength ranges, owing to their unique anisotropic structures [37–40]. Yet, to date, broadband polarization-sensitive photodetectors based on a single material—particularly those exhibiting spectral selectivity across visible and infrared bands—have been rarely reported. This is despite the considerable potential such devices hold for processing multidimensional optical information efficiently. Additionally, the photothermoelectric (PTE) effect, driven by light-induced temperature gradients, enables bipolar photocurrent modulation purely in response to optical stimuli [41–44]. This mechanism effectively eliminates the need for external electrical gating and offers significant advantages for in-sensor computing applications. Consequently, by strategically leveraging anisotropic 2D materials that combine spectral selectivity and polarization sensitivity with bipolar photocurrent modulation via the PTE effect, multidimensional optical features can be efficiently extracted through the deliberate development of computational optoelectronic devices. Critically, the development of novel 2D materials is urgently required as the pivotal breakthrough to enable the seamless co-existence of polarization-resolved and spectrum-selected detection capabilities within a unified, low-power PTE platform.

In this work, the 2D tri-$HfGeTe_4$, with its low-symmetry puckered structure of trigonal and tetragonal rings, is introduced for self-powered in-sensor multidimensional computing. Interestingly, it is, to our knowledge, the first report of trigonal building units in 2D materials. It is worth noting that the structural in-plane anisotropy and narrow bandgap (0.6 eV) of tri-$HfGeTe_4$ enable broadband polarization-sensitive photodetection (405-1064 nm), yielding anisotropy ratios of up to 2.08 (671 nm) and 1.86 (1064 nm). Remarkably, the dominant polarization orientation shifts by 90° between the visible and near-infrared bands, revealing distinct spectral selectivity. Distinguished by its pronounced polarization sensitivity and unique spectral selectivity, the tri-$HfGeTe_4$ device permits the capture of multidimensional optical information. In addition, relying on the PTE effect, it enables bipolar photocurrent modulation at zero bias, supporting in-sensor computing for feature extraction. Combined with neural networks, the device achieves more precise target recognition—reaching 91% IoU in semantic segmentation. This advance demonstrates the potential of in-plane anisotropic 2D tri-$HfGeTe_4$ for efficient multidimensional visual processing without complex hardware.

2 | Results and Discussion

2.1 | Principles of In-Sensor Multidimensional Visual Information Perception

The conceptual framework for in-sensor multidimensional visual information processing leverages computational photodetectors capable of simultaneously responding to both infrared and visible light inputs, while also detecting variations in polarization states (Figure 1a). By employing reconfigurable photoresponsivities as operational kernels, the system encodes the full multidimensional optical information matrix—rather than isolating individual dimensions—into a unified output (Figure 1b). This approach enables the mapping of complete visual scenes and facilitates the extraction of targeted features (Figure 1c). These unique capabilities stem from the synergistic integration of key physical properties inherent in the underlying 2D tri-$HfGeTe_4$ material (Figure 1d). Specifically, tri-$HfGeTe_4$ exhibits pronounced in-plane structural anisotropy, leading to polarization-dependent optical behaviors that establish multiple distinguishable response states. Furthermore, the material demonstrates a unique spectrally selective polarization-sensitive behavior spanning from visible to near-infrared light, the dominant polarization orientations at these two wavelengths are orthogonal to each other, which greatly facilitates dual-band information discrimination.

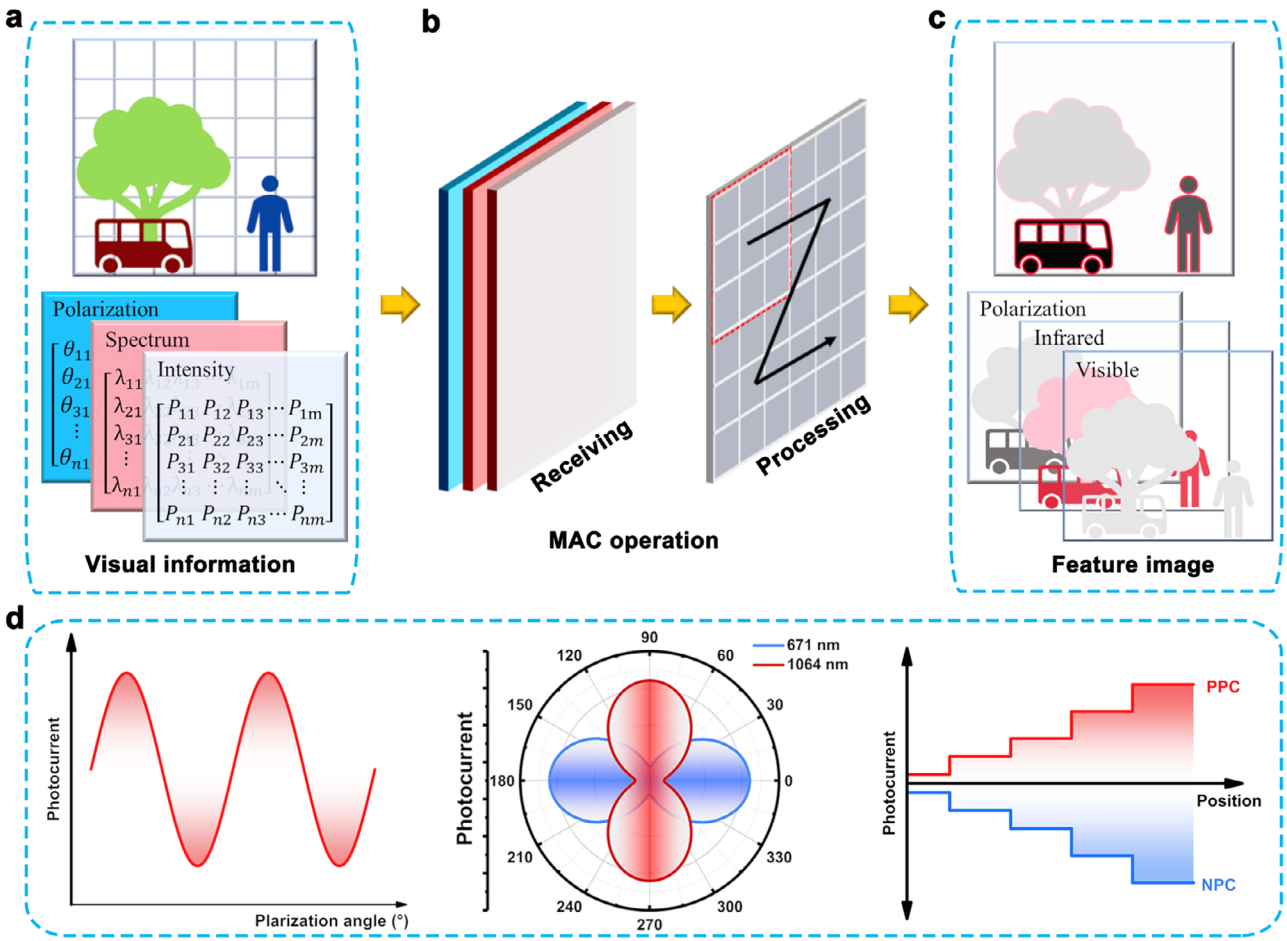

FIGURE 1 | Principles of in-sensor multidimensional visual information processing. (a) The input visual scene and the multidimensional visual information matrix. (b) MAC operation, including multidimensional visual information perceiving and processing. (c) The output structured features. (d) Polarization sensitivity and spectral selectivity, as well as controllable bipolar photoresponse based on PTE operations.

At the same time, the PTE effect endows the device with both self-powered operation and tunable bipolar photoresponse characteristics, that is, positive photocurrent (PPC) and negative photocurrent (NPC). To illustrate the practical relevance of such a system, consider a scene containing a person, a car, and a tree. Its accurate and comprehensive representation relies on the effective integration of multidimensional optical information (Figure 1a–c). If only the spatial distribution of visible light intensity is captured, other critical optical features are lost, thereby limiting the accuracy and robustness of object detection and recognition—particularly under complex lighting conditions. In real-world scenarios, the ability to sense infrared radiation significantly enhances the detection of objects such as people and cars. Meanwhile, polarization-sensitive photoresponse further helps to establish distinguishable intensity profiles among different objects within the scene. As a result, by concurrently detecting visible light, infrared radiation, and polarization states, the sensor achieves a more holistic perception of the scene. This integrated sensing strategy not only supports a differentiated representation of various objects based on their brightness patterns in space, but also markedly improves overall image contrast.

2.2 | Anisotropic Crystal Structure and Optical Properties of 2D tri-$HfGeTe_4$

Tri-$HfGeTe_4$ crystallizes in a novel, low-symmetry, puckered layered structure (Figure 2a), which is characterized by a non-centrosymmetric orthorhombic space group ($Cmc2_1$) and lattice parameters $a = 3.9892(17)$ Å, $b = 15.972(7)$ Å, and $c = 10.982(4)$ Å [45]. In contrast to the symmetric, planar structures of typical 2D materials, tri-HfGeTe4 forms a periodically corrugated monolayer with a thickness of 7.79 Å (Figure 2a and Figure S1). Notably, the intrinsically puckered, asymmetric layers are composed of both trigonal and tetragonal motifs, marking, to our knowledge, the first observation of trigonal motifs in 2D materials (Figure 2b). Based on this, the 2D material $HfGeTe_4$ is named 2D tri-$HfGeTe_4$. The structural diversity of tri-HfGeTe4's triangular and tetragonal units results in an intrinsically anisotropic, low-symmetry crystal. This structural anisotropy directly confers significant polarization sensitivity, manifesting as distinct in-plane anisotropy in both its optical and optoelectronic properties. High-quality bulk single crystals of tri-$HfGeTe_4$ (Figure S2) were successfully synthesized via solid-state reactions, as described in the experimental section. Subsequently, the phase purity of the as-synthesized

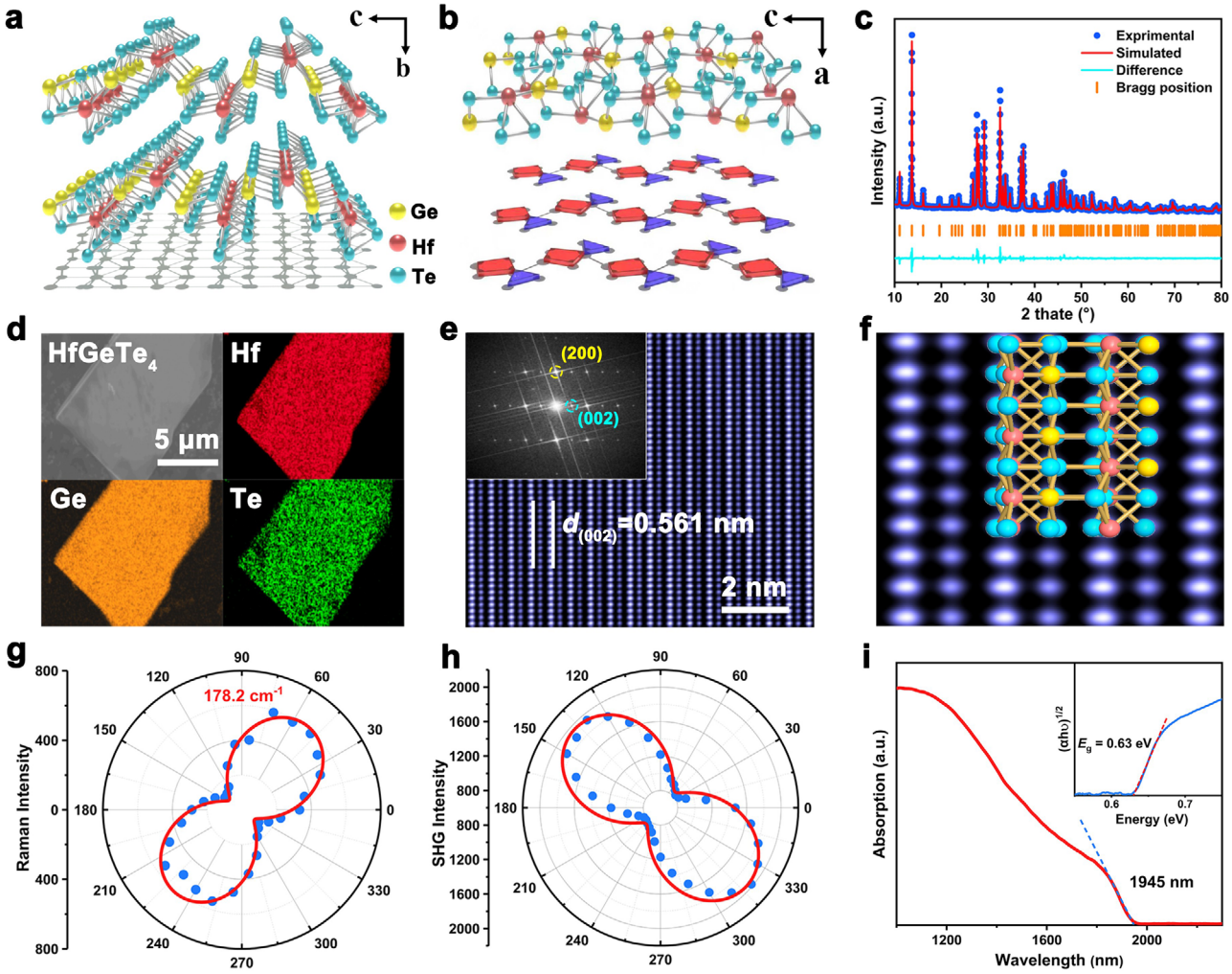

FIGURE 2 | Anisotropic crystal structure and optical properties of 2D tri-$HfGeTe_4$. (a) Schematic illustration of the atomic structure of tri-$HfGeTe_4$ viewed along the *a*-axis. (b) The atomic projection diagram along the *a*-axis, including intrinsically anisotropic trigon and tetragon motifs. (c) Experimental and simulated XRD patterns of tri-$HfGeTe_4$ single crystals. (d) EDS elemental mapping of tri-$HfGeTe_4$ flake. (e) Atomically resolved HAADF image and the corresponding SAED pattern in the inset. (f) The enlarged HAADF image, together with the corresponding top-view atomic model. (g) Anisotropic Raman intensities (178.2 cm^{-1}) under parallel configurations. (h) Polarization-dependent SHG signals. (i) UV–vis–NIR absorption spectrum and extracted *Tauc*-curve (inset) of tri-$HfGeTe_4$.

crystals was confirmed by powder X-ray diffraction (XRD), in which the experimental pattern aligns closely with the theoretical simulation (Figure 2c). Furthermore, energy dispersive X-ray spectroscopy (EDS) mapping (Figure 2d) reveals a uniform distribution of Hf, Ge, and Te throughout the sample, with an atomic ratio consistent with the stoichiometric proportion of 1:1:4 (Figure S3), thereby corroborating the successful synthesis. To further probe the in-plane structural anisotropy and crystalline quality, we employed scanning transmission electron microscopy (STEM) to analyze the atomic structure of few-layer tri-$HfGeTe_4$. The selected-area electron diffraction (SAED) pattern (inset of Figure 2e) exhibits a single set of diffraction spots, which can be unambiguously indexed to an orthorhombic crystal system. Additionally, atomically resolved high-angle annular dark-field (HAADF) imaging (Figure 2e) clearly reveals the (002) lattice fringes, measured to be 0.561 nm. More importantly, the HAADF image enables direct visualization of the in-plane anisotropic arrangement of atomic dots, along with precise structural matching (Figure 2f). In summary, through comprehensive material characterization—including XRD, EDS, SAED, and HAADF-STEM—we have unequivocally confirmed the anisotropic crystal structure and high crystalline quality of the synthesized tri-$HfGeTe_4$ flakes.

The inherent anisotropic structure of tri-$HfGeTe_4$ gives rise to polarization-dependent optical properties, leading to a range of intriguing linear and nonlinear optical phenomena. To clarify the relationship between structural anisotropy and optical anisotropy in 2D tri-$HfGeTe_4$, we carried out systematic optical characterization. Under parallel configuration, nine distinct Raman peaks were clearly observed (Figure S4), and their intensities showed periodic variation with the polarization angle (Figure S5). To further analyze the anisotropic phonon vibrations, we fitted the polarized angle-resolved Raman intensity using the equation described in Note S1. As a result, the peaks at 76.7 and 150.1 cm^{-1} exhibited a four-lobe polar pattern (A_2 mode), whereas the other peaks (90.7, 101.8, 140.1, 178.2, 196.6, and 229.3 cm^{-1}) displayed a two-lobe polar pattern corresponding to the

A_1(z) mode (Figure 2g and Figure S6). These findings confirm distinct in-plane vibrational anisotropy along different crystal orientations. Furthermore, the non-centrosymmetric structure of 2D tri-$HfGeTe_4$ enables second-order nonlinear optical effects, such as second-harmonic generation (SHG, $\lambda_{pump} = 2\lambda_{SHG}$). When excited by a 1040 nm laser at room temperature, the SHG spectrum of the sample showed a clear peak at 520 nm (Figure S7). Moreover, the polarized angle-resolved SHG signals revealed a two-fold symmetric pattern, accurately reflecting the underlying two-fold rotational symmetry and in-plane anisotropy of 2D tri-$HfGeTe_4$ (Figure 2h). In addition, we employed azimuth-dependent reflectance difference microscopy (ADRDM) to directly visualize the in-plane anisotropic optical properties of tri-$HfGeTe_4$. In ADRDM images taken at angles from 0° to 180°, the color of the tri-$HfGeTe_4$ flakes changed significantly, while the isotropic SiO_2/Si substrate showed no notable polarization dependence (Figure S8). Correspondingly, the angle-dependent reflectance difference signals of tri-$HfGeTe_4$ exhibited periodic oscillations (Figure S9 and Note S2), further underscoring its pronounced in-plane optical anisotropy. Additionally, our experimental measurements reveal for the first time that tri-$HfGeTe_4$ possesses a relatively narrow bandgap of 0.6 eV (Figure 2i), suggesting its potential for broadband photoresponse across visible to near-infrared wavelengths. Consequently, these combined attributes make it a promising candidate for multimodal visual information perception.

2.3 | Optoelectronic Characteristics of 2D tri-$HfGeTe_4$

To demonstrate in-sensor multidimensional visual perception as illustrated in Figure 1, we employed a photodetector based on as-grown tri-$HfGeTe_4$ to realize broadband and polarization-dependent photoresponse, as well as tunable photoresponsivity. The device was constructed by mechanically exfoliating a tri-$HfGeTe_4$ flake and dry-transferring it onto pre-patterned Au electrodes on a Si/SiO_2 substrate (Figure 3a). Further fabrication details are provided in the experimental section. The negative temperature-dependent resistance confirms the semiconducting nature of tri-$HfGeTe_4$ (Figure S10), and the linear *I–V* curve demonstrates ohmic contact at the electrode–semiconductor interface (Figure S11). Under uniform illumination at 671 nm, the device exhibits a clear photoresponse, featuring an open-circuit voltage (V_{oc}) of -0.1 mV and a short-circuit current (I_{sc}) of 10 nA (Figure 3b). Notably, both V_{oc} and I_{sc} reverse polarity when the laser spot is shifted from one end of the device to the other—a key feature enabling photoresponsivity tuning. Additionally, the device resistance remains constant even when the light intensity changes, which is consistent with the PTE effect [43, 44]. Owing to the narrow bandgap of tri-$HfGeTe_4$, the device operates stably at zero bias and achieves self-powered broadband detection from visible to near-infrared wavelengths (Figure 3c). To ensure the practical application of our devices, we investigated the cyclic and environmental stability of the tri-$HfGeTe_4$ device. It is also noted that the devices maintain reproducible photoresponse characteristics after more than 500 cycles, with less than approximately a 5% decrease in photocurrent, as shown in Figure 3d. As shown in Figure S12a, after the sample was placed in the environmental air for 6 months, no significant degradation in its photocurrent was observed. In addition, the device shows an on/off ratio of ~3.3×10^2 and a fast response with rise and decay times of ~27 and ~33 ms, respectively (Figure S12b). Time-resolved photocurrent measurements under varying laser power (Figure S13) reveal that the photocurrent (I_{ph}) scales nearly linearly with light intensity (P), following the power law $I_{ph} \propto P^{\alpha}$ [23], where $\alpha \approx 1$ (Figure 3e and Figure S14). This linear photocurrent–intensity relationship is essential for in-sensor image processing. Responsivity ($R = I_{ph}/P$) [46] was also evaluated (Figure S15), and the values at maximum intensity are plotted in Figure 3f, showing a tunable range of ± 0.3 mA/W depending on the PTE operation mode. These results confirm that the photoresponse is primarily thermally driven rather than due to direct carrier excitation.

Scanning photocurrent mapping (SPCM) was performed at room temperature to further study the photocurrent generation mechanism. The SPCM results (Figure 3g and Figure S16) exhibit an opposite photocurrent at the two ends of the channel, and a region near the center of the channel exists where $I_{ph} = 0$. The photocurrent distribution mainly occurs at the interface between the tri-$HfGeTe_4$ light-absorbing layer and the Au electrodes, as well as in the regions flanking the electrodes. In photocurrent generation, three mechanisms operate under unbiased conditions [43, 44, 47–49]: the photovoltaic (PV) effect, the bulk photovoltaic effect (BPVE), and the PTE effect. The PV effect relies on a built-in electric field from Schottky contacts, producing a nonlinear *I-V* curve and a localized photocurrent near the junction. However, our device shows a linear *I–V* curve and a broad photocurrent distribution, ruling out the PV mechanism. In BPVE, the photocurrent typically peaks within the channel material without polarity reversal as the light spot moves. By contrast, our device exhibits maximum photocurrent at the contacts with opposite polarities, excluding BPVE. The PTE effect, on the other hand, yields both a linear *I-V* response and a nonlocal photocurrent, consistent with our observations. The photocurrent generated in the tri-$HfGeTe_4$ device originates from incident photons that create spatially localized thermal gradients. Figure 3h shows the position-dependent photocurrent, which was tested by gradually moving the light spot (0.5 μm per step) from one end to the other of the device. Benefiting from this continuous position-dependent photoresponse, both enhancement and suppression of photoresponsivity can be flexibly regulated. More importantly, it provides more weights for the convolution operation. The power-dependent photocurrent curves (Figure 3i) under different laser irradiation positions were extracted by Figure 3h. The linear curve satisfies the requirements for convolution processing and allows for the photocurrent to be mapped according to different sets of convolution weights.

Building on the established in-plane optical anisotropy and broadband photoresponse of tri-$HfGeTe_4$, we further investigated its polarization-sensitive photocurrent characteristics. Specifically, the polarization angle is defined as 0° when it is parallel to the material's long side, and the linear polarization angle is rotated from 0° to 360° in 20° steps. As shown in Figure S17, the photocurrent clearly exhibits pronounced periodic modulation with changing the angle of linearly polarized light. For comparison, Figure 4a–c show the polar plots of the angle-resolved photocurrent under laser irradiation at 405, 473, 532, 671, and 1064 nm. The clear two-lobed pattern aligns with the optical anisotropy and is attributable to the material's intrinsic structural anisotropy. The dichroic ratio ($I_{ph,max}/I_{ph,min}$) consistently exceeds

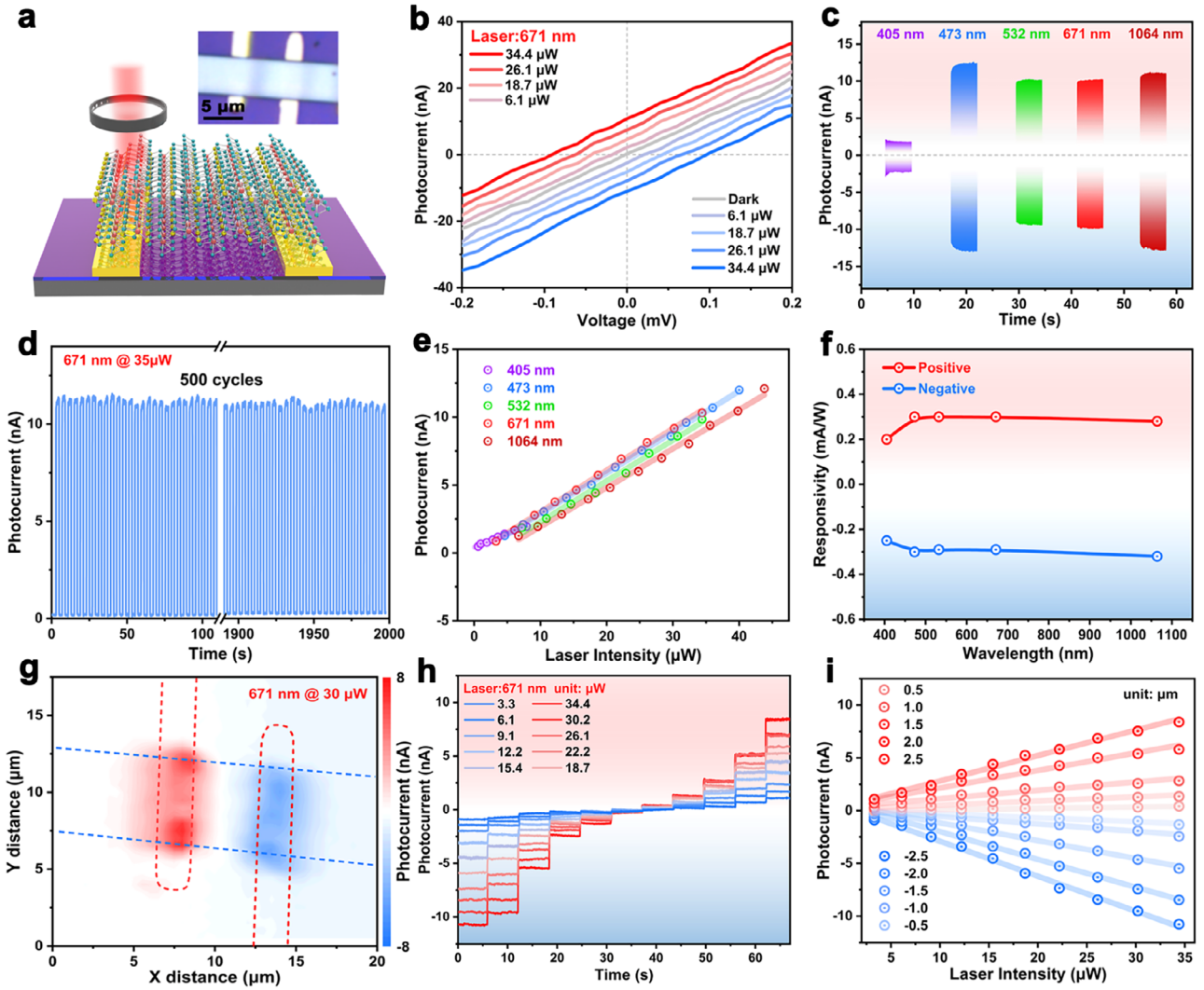

FIGURE 3 | Optoelectronic characteristics of 2D tri-$HfGeTe_4$. (a) Schematic diagram and the optical image of the tri-$HfGeTe_4$ photodetector. (b) *I–V* curves under the irradiation of 671 nm laser (red and blue) and the dark condition (gray). (c) Broadband photoresponse under different wavelengths of laser. (d) Photoresponse cycle stability of tri-$HfGeTe_4$ device under alternating on/off cycles. (e) Positive photocurrent as a function of light intensity. (f) The wavelength-dependent responsivity was extracted by Figure S12, with each value corresponding to the responsivity at the maximum laser intensity. (g) SPCM under the irradiation of 671 nm. (h) The position-dependent photocurrent under different laser intensity. (i) The linear power-dependent photocurrent curves under different laser irradiation positions were extracted by Figure 3h.

1.5 across a broad spectral range from visible to near-infrared, reaching up to 2.08 at 671 nm. These results highlight the excellent performance of the tri-$HfGeTe_4$ device in polarization-sensitive photodetection, and are highly comparable to those of other 2D anisotropic semiconductors, including bAs [50], $PdSe_2$ [37], $NbOI_2$ [51], PdPS [52]. Interestingly, under near-infrared laser irradiation, the dominant polarization orientation rotates by 90° compared to that observed under visible light illumination. This distinct spectrally selective polarization-sensitive behavior allows the device to effectively capture spectral information, thereby providing deeper insights into complex scenes. Importantly, the power-dependent photocurrent exhibits distinct linear relationships at various polarization angles (Figure 4d,e), thereby enabling clearly distinguishable response states among scene elements. Furthermore, the polarization-sensitive behavior can be effectively combined with PTE operations to achieve precisely controllable photoresponse (Figure 4f). This capability is particularly essential for applications in polarization-sensitive in-sensor computing vision systems aimed at advanced image processing.

The polarization state of reflected light varies depending on the object's interaction with the incident light. Therefore, by utilizing the photocurrent difference of the device under different polarization states, it offers great potential for enhancing target brightness differentiation and improving contrast between the target and background. The schematic diagram comparing normal and polarized images is shown in Figure S18. For the tri-$HfGeTe_4$ device, its intrinsic structural anisotropy gives rise to angle-resolved photocurrent. In order to demonstrate the contrast enhancement of polarized images, we correlated the polarized photocurrent ($I_{0°}$ for target, $I_{90°}$ for background) with the gray gradient (ranging from 0 to 255). The mapping relationship is extracted from Figure 4d. Figure 4g,h present the normal and enhanced-contrast polarized image, respectively. The polarized image shows superior contrast and

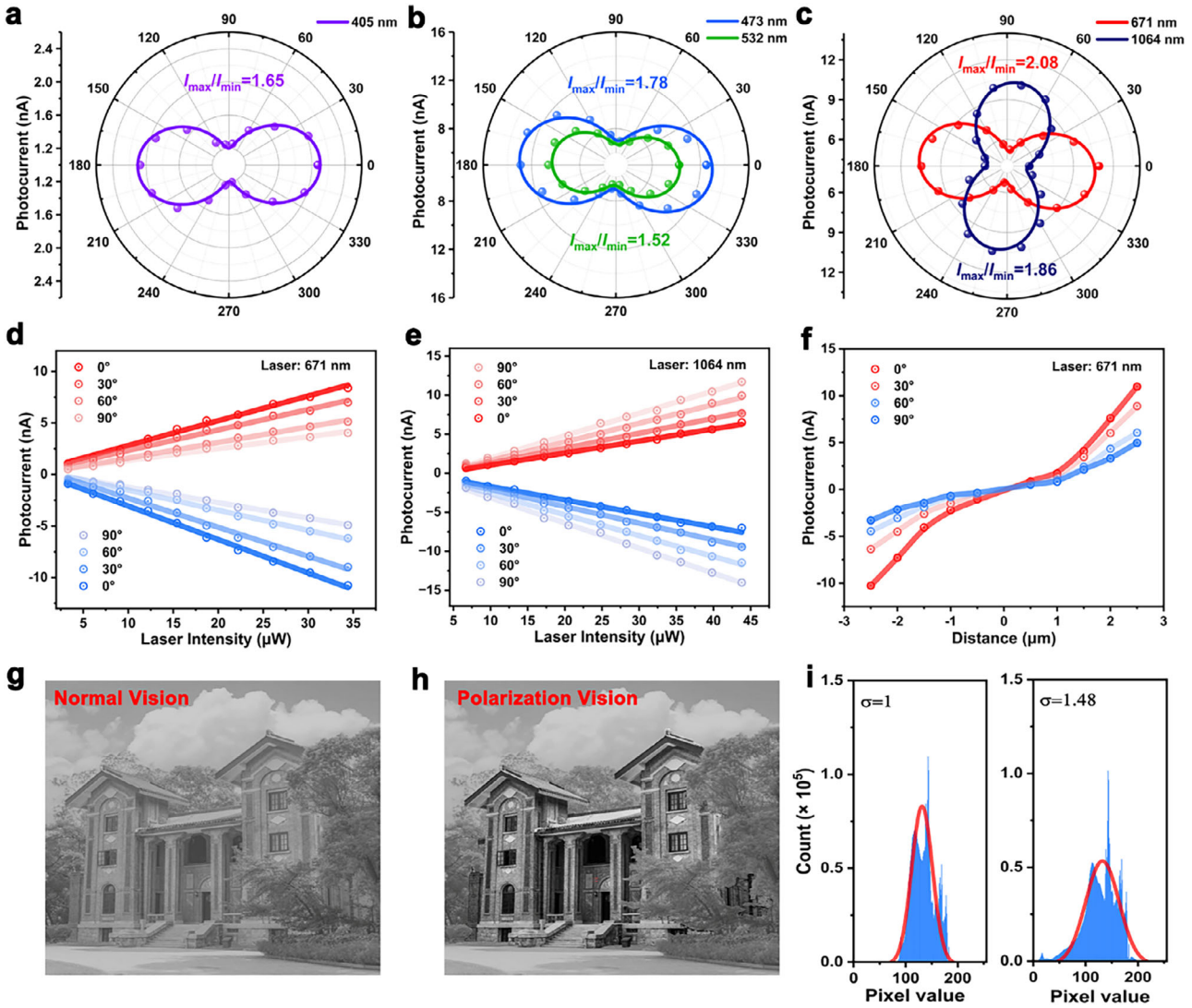

FIGURE 4 | Polarization-sensitive optoelectronic response of 2D tri-$HfGeTe_4$. (a–c) Angle-resolved I_{ph} under (a) 405 nm, (b) 473 and 532 nm, and (c) 671 and 1064 nm, respectively. (d, e) The power-dependent I_{ph} curves under different polarization angles at 671 and 1064 nm, respectively. (f) The position-dependent I_{ph} curves under different polarization angles at 671 nm. (g, h) Demonstration of polarization image enhancement after strengthening the contrast ratio of targets. (i) Pixel intensity distribution histograms corresponding to Fig 4g and Fig 4h, respectively.

structural clarity. Comparative analysis of the pixel distribution histograms reveals that the polarized image exhibits a broader distribution range than the normal image, indicating that it captures more effective information. Meanwhile, the relative standard deviation (σ) is used to measure the effect of image enhancement, in which a high σ value indicates a greater contrast between the foreground and the background. The image contrast of the polarized image is markedly higher than that normal image, underscoring the critical role of the polarizing device in retrieving meaningful information from complex environments.

2.4 | In-Sensor Multidimensional Image Processing and Segmentation Tasks

Building on the demonstrated self-powered broadband polarization-resolved and spectrum-selective photoresponse, as well as the controllable bipolar PTE behavior, tri-$HfGeTe_4$ devices become feasible to achieve in-sensor image processing and semantic segmentation tasks. Here, the Deeplab V3+ model was employed for the semantic segmentation task, and detailed description can be found in the Supporting information (Note S3). Among ASPP module can enlarge the receptive field and capture multi-scale image information more efficiently with reduced computational steps (Figure S19). The input to the object detection network consists of multidimensional optical information—encompassing intensity distribution, spectral composition, and polarization state—while the output is a semantic segmentation map color-coded by object category (Figure 5a). Currently, we have fabricated and tested a single tri-$HfGeTe_4$ device, but the pixelated focal plane array is still under development. To evaluate the potential of this device in in-sensor multidimensional perception, we adopted a physical principle-based simulation framework (Figure 5b). This framework models the device's spectral and polarization responses using experimentally verified data and applies it to each pixel of the image dataset to generate a four-channel input. A detailed

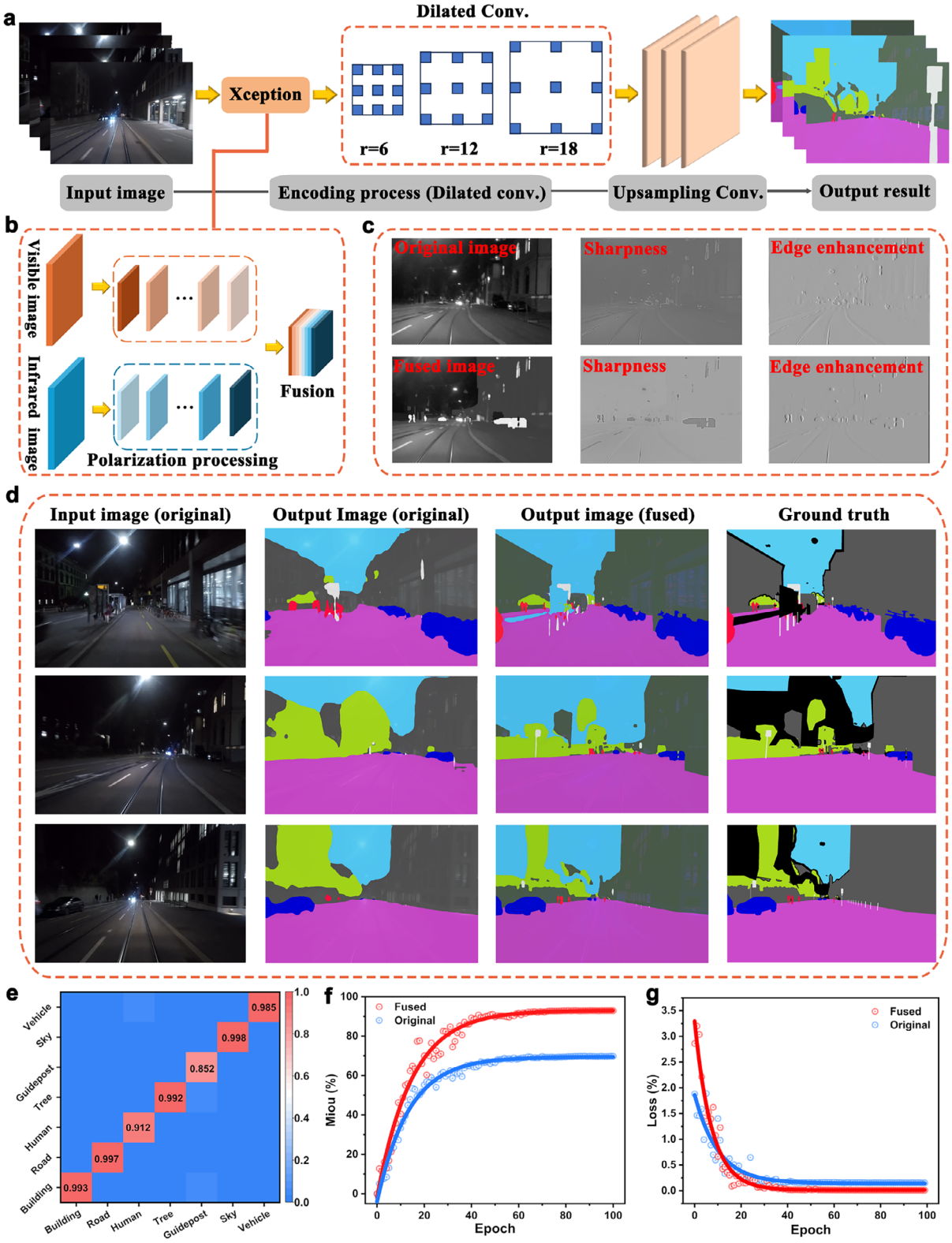

FIGURE 5 | Multidimensional image processing and segmentation tasks based on 2D tri-$HfGeTe_4$ devices. (a) Flowchart of image processing and segmentation using dilated convolution. (b) The process of data fusion operation based on 2D tri-$HfGeTe_4$ devices. (c) Demonstration of image convolutional processing, and the experimental results using original image (top) are compared with fused image (bottom). (d) Partial input images used for testing (ACDC dataset). Semantic segmentation results based on original image and fused image, and the labels corresponding to the input images. (e) Confusion matrix of semantic segmentation using dilated convolution based on fused image. (f) Comparison of semantic segmentation IoU values based on original image and fused image. (g) Comparison of semantic segmentation loss values.

description of the data fusion pipeline has been added to the Supporting Information (Note S4).

For in-sensor multidimensional visual perception and convolution operations, we used a street view image from the ACDC dataset containing seven endmembers [53]. Notably, different types of information within the image are accentuated across distinct optical dimensions. Specifically, features such as "building", "road", "tree", "guidepost", and "sky" are primarily highlighted in the visible band, whereas "human" and "vehicle" are more distinct in the NIR band. Moreover, polarization variations among different scene components enable differentiated feature intensity expression, thereby enhancing inter-class contrast. To validate the effectiveness of multidimensional visual perception, we compared convolution results from original, single-channel, and fused grayscale images. By modulating the tri-$HfGeTe_4$ device's responsivity, various convolution kernels (3×3, $r = 1$) with distinct responsivity profiles were implemented (Figure S20). These kernels successfully performed sharpening and edge enhancement. The results of the original image (visible) and multidimensional perception convolution are presented in Figure 5c, with the multidimensional approach consistently outperforming the original image. Compared to the original image, the fused version offers richer contextual features, with target objects exhibiting clearer features and sharper edges. Additional visualizations across different optical dimensions are provided in Figure S21, each capturing unique characteristics of the scene components. By integrating information across multidimensional optical dimensions, more comprehensive scene perception and clear inter-class contrast are achieved. Overall, these computational results highlight the promising potential of in-sensor multidimensional visual perception devices for efficient and compact computing in tasks such as holistic scene interpretation and target recognition.

Further, leveraging the multidimensional perception capability and scalable convolution kernels, the utility of our device extends beyond image convolution processing, demonstrating considerable promise in semantic segmentation tasks. As a core task in computer vision, semantic segmentation assigns a specific category label—such as "person," "car," "tree," or "sky"—to each pixel in an image [54]. In contrast to object detection, which localizes targets using bounding boxes, semantic segmentation achieves pixel-level dense prediction, thereby accurately delineating object contours and generating machine-readable, pixel-wise semantic maps. By incorporating multidimensional visual data (Figure 5d), segmentation networks can acquire a more comprehensive scene representation, leading to significantly improved accuracy and robustness across diverse and challenging environments. As illustrated in Figure 5d, which compares the original input image, segmentation output results based on original and fused images, and the ground truth, our approach markedly enhances segmentation clarity for objects such as buildings, roads, humans, and vehicles. To quantitatively evaluate segmentation performance, we employed the Intersection over Union (IoU) metric. IoU measures the overlap between predicted and ground truth segmentations, normalized by their union. Mathematically, it is defined as: $IoU = |P \bigcap G| \; |P \bigcup G|$, where P represents the set of pixels predicted as the object, G denotes the ground truth pixels, $|P \bigcap G|$ is the area of overlap, and $|P \bigcup G|$ is the total area covered by both. IoU values range from 0 to 1, with values closer to 1 indicating higher segmentation accuracy. The confusion matrix from semantic segmentation using dilated convolution based on our tri-$HfGeTe_4$ devices (Figure 5e), reveals a high object recognition rate and excellent segmentation performance, underscoring the potential advantages of multidimensional perception in image segmentation applications. Finally, we compared object detection performance using two types of inputs: visible-spectrum-only images versus those incorporating fused light intensity, spectral, and polarization data. Due to the limited global feature perception, the model trained with non-fused data only can achieve a moderate accuracy. In contrast, multidimensional visual feature fusion learning attains an accuracy of 91% (Figure 5f), accompanied by consistently minimized training loss (Figure 5g). In summary, 2D tri-$HfGeTe_4$ devices effectively enable self-powered image perception and high-performance semantic segmentation, demonstrating strong potential for real-world vision systems.

3 | Conclusion

In summary, we developed 2D tri-$HfGeTe_4$ computational device capable of polarization-resolved, spectrum-selective detection and zero-power operation, which achieves direct multidimensional visual perception within a single image frame without requiring multi-frame capture or off-chip computation. By integrating the narrow optical bandgap and in-plane anisotropy of 2D tri-$HfGeTe_4$, the developed devices exhibit broadband polarization-sensitive responses across 405–1064 nm, with high anisotropy ratios of 2.08 at 671 nm and 1.86 at 1064 nm. Notably, the devices also exhibit a unique spectrally selective polarization-sensitive behavior, further allowing it to capture multidimensional visual information. Furthermore, leveraging the PTE effect, these devices also achieve a self-powered and controllable bipolar photoresponse. These outstanding properties of the 2D tri-$HfGeTe_4$ computational platform allow for the direct encoding and integration of spectral, polarization, and luminance data during photoexcitation. More importantly, through integration with neural networks in a semantic segmentation task, such a system achieves more accurate target recognition with a high IoU of 91%. Our findings establish in-sensor multidimensional visual perception as a compact, efficient, and scalable solution for next-generation vision systems, paving the way for its application in autonomous sensing and edge neuromorphic computing.

4 | Experimental Section

4.1 | Growth of 2D tri-$HfGeTe_4$ Crystals

Single crystals of 2D tri-$HfGeTe_4$ were successfully synthesized via high-temperature solid-state reactions. The process began by thoroughly mixing high-purity hafnium (Hf), germanium (Ge), and tellurium (Te) powders in stoichiometric proportions. The mixture was then sealed in an evacuated quartz ampule under a vacuum of 10^{-6} Torr and heated in a furnace from room temperature to 923 K at a rate of 20 K/h. After maintaining this temperature for 120 h, the furnace was gradually cooled to room temperature over a period of 24 h. At last, bulk black single crystals of tri-$HfGeTe_4$ were successfully obtained.

4.2 | Characterizations of 2D tri-$HfGeTe_4$

The powder XRD pattern was recorded using an X-ray diffractometer (D/MAX-2200, Rigaku, Cu-K_α radiation) from 10° to 80° with a step of 0.02°. SEM images and EDX spectroscopy were collected using a HITACHI Regulus 8230. Tri-$HfGeTe_4$ flakes were exfoliated and transferred (by conventional wet-transfer method) onto a Cu grid with a carbon film, and HAADF and SAED were then obtained by using STEM (Tecnai G2 F30). Under a parallel-polarized configuration, the polarization-resolved Raman spectra were measured using a Raman spectrometer (Xplora Plus, HORIBA) with a 532 nm laser of a diameter of 1 μm, and the sample was rotated anticlockwise from 0° to 360° with a step of 12°. SHG signal was excited by using a commercial Ti: Sapphire femtosecond laser (Coherent), and collected using a confocal microscopy spectrometer (Alpha 300RS+, WITec). An additional half-wave plate was used to control the polarization angle with a step of 10°, and the horizontal direction is defined as 0°. Optical anisotropic images were obtained by using a ADRDM equipped with a linear polarizer and a liquid crystal variable retarder. The reflected light was collected by the same objective, and the reflectance difference signal was solved by the light intensity on the CCD detector. Using Ba_2SO_3 as a standard sample, the absorption spectrum was recorded using the UV–vis–NIR photometer (Perkin-Elmer, Lambda950) at room temperature, and the band gap was calculated according to the *Tauc* equation: $(h\nu\alpha)^{1/2} = A(h\nu - E_g)$.

4.3 | Device Fabrication and Measurements

Ti/Au electrodes (10 nm/70 nm) were fabricated on a SiO_2/Si substrate by combining optical maskless lithography (μPG 501, Heidelberg) with high-vacuum thermal evaporation (DE 400, Wavetest). Tri-$HfGeTe_4$ flakes were mechanically exfoliated from bulk single crystals and transferred onto the Au electrodes via a polydimethylsiloxane (PDMS)-assisted dry transfer process. Temperature-dependent resistance measurements were performed in a physical property measurement system (PPMS DynaCool, Quantum Design). Optoelectrical characterizations were carried out using an integrated optical-electrical assembly, which included semiconductor parameter analyzers (Keithley 4200 and Keithley 2400), monochromatic lasers (405, 473, 532, 671, and 1064 nm), a microscope equipped with a CCD camera, a programmable displacement stage, and various optical components. All measurements were conducted using a 100× objective lens to focus the laser onto the device, yielding a laser spot diameter of 5 μm. For position-dependent photocurrent mapping, the device was moved horizontally in 0.5 μm steps. Polarization-dependent photocurrent was measured by rotating a half-wave plate, and the resulting signal was recorded with a Keithley 4200. Scanning photocurrent microscopy (SPCM) (TuoTuo Technology, TTT-03-PC) was implemented by controlling the device position with the programmable stage.

Acknowledgements

This work was supported by the National Key Research and Development Program of China (No. 2021YFA1200903), the National High-Level Talents Special Support Program—Young Talents (2025WRQB007), the National Natural Science Foundation of China (Nos. 22576040, 22175203, 22006023, and 11974435), and Guangzhou Science and Technology Project (No. 202102020126).

Conflicts of Interest

The authors declare no conflicts of interest.

Data Availability Statement

The data that support the findings of this study are available from the corresponding author upon reasonable request.

References

1. C. He, Y. Shen, and A. Forbes, "Towards Higher-Dimensional Structured Light," *Light: Science & Applications* 11 (2022): 205, https://doi.org/10.1038/s41377-022-00897-3.

2. Z. Wang, T. Wan, S. Ma, and Y. Chai, "Multidimensional Vision Sensors for Information Processing," *Nature Nanotechnology* 19 (2024): 919–930, https://doi.org/10.1038/s41565-024-01665-7.

3. F. Wang, S. Fang, Y. Zhang, and Q. J. Wang, "2D Computational Photodetectors Enabling Multidimensional Optical Information Perception," *Nature Communications* 16 (2025): 6791, https://doi.org/10.1038/s41467-025-61924-6.

4. S. Zhang, H. Jiao, Y. Chen, et al., "Multi-Dimensional Optical Information Acquisition based on a Misaligned Unipolar Barrier Photodetector," *Nature Communications* 15 (2024): 7071, https://doi.org/10.1038/s41467-024-51378-7.

5. Z. Shen, F. Zhao, C. Jin, S. Wang, L. Cao, and Y. Yang, "Monocular Metasurface Camera for Passive Single-Shot 4D Imaging," *Nature Communications* 14 (2023): 1035, https://doi.org/10.1038/s41467-023-36812-6.

6. F. Wang, S. Zhu, W. Chen, et al., "Multidimensional Detection Enabled by Twisted Black Arsenic–Phosphorus Homojunctions," *Nature Nanotechnology* 19 (2024): 455–462, https://doi.org/10.1038/s41565-023-01593-y.

7. A. Hwang, M. Park, Y. Park, et al., "Visible and Infrared Dual-Band Imaging via Ge/MoS2 van der Waals Heterostructure," *Science Advances* 7 (2021): abj2521.

8. K. D. Hakkel, M. Petruzzella, F. Ou, et al., "Integrated Near-Infrared Spectral Sensing," *Nature Communications* 13 (2022): 103, https://doi.org/10.1038/s41467-021-27662-1.

9. Z.-A. Li, C. Pan, P. Wang, et al., "In-Pixel Dual-Band Intercorrelated Compressive Sensing Based on MoS 2 /h-BN/PdSe 2 Vertical Heterostructure," *ACS Nano* 19 (2025): 6263, https://doi.org/10.1021/acsnano.4c15453.

10. D. Ouyang, M. Wang, N. Zhang, et al., "2D Time-Stretching Anisotropic Synapse Realizing In-Sensor Intensity-Spanning Visual Feature Fusion," *Advanced Materials* 37 (2025): 2507168, https://doi.org/10.1002/adma.202507168.

11. Y. Yang, W. Ran, Y. Li, Y. Chen, D. Chen, and G. Shen, "Multi-Dimensional Visual Information Processing Under Complex Light Environments Using Time-Evolved Polarization-Sensitive Synaptic Electronics," *Nature Communications* 16 (2025): 5665, https://doi.org/10.1038/s41467-025-61361-5.

12. T. Guo, S. Li, Y. N. Zhou, W. D. Lu, Y. Yan, and Y. A. Wu, "Interspecies-Chimera Machine Vision with Polarimetry for Real-Time Navigation and Anti-Glare Pattern Recognition," *Nature Communications* 15 (2024): 6731, https://doi.org/10.1038/s41467-024-51178-z.

13. S. Chen, S. Chen, X. Chen, et al., "Neuromorphic Polarization Vision Enabled by Organic Single-Crystal Photosynaptic Transistors," *Advanced Materials* 37 (2025): 2505491, https://doi.org/10.1002/adma.202505491.

14. H. H. Yoon, H. A. Fernandez, F. Nigmatulin, et al., "Miniaturized Spectrometers with a Tunable Van Der Waals Junction," *Science* 378 (2022): 296–299.

15. W. Xin, W. Zhong, Y. Shi, et al., "Low-Dimensional-Materials-Based Photodetectors for Next-Generation Polarized Detection and Imaging," *Advanced Materials* 36 (2023): 2306772, https://doi.org/10.1002/adma.202306772.

16. Y. Chai, "In-Sensor Computing for Machine Vision," *Nature* 579 (2020): 32–33, https://doi.org/10.1038/d41586-020-00592-6.

17. F. Zhou and Y. Chai, "Near-Sensor and In-Sensor Computing," *Nature Electronics* 3 (2020): 664–671, https://doi.org/10.1038/s41928-020-00501-9.

18. N. Goel and R. Kumar, "Physics of 2D Materials for Developing Smart Devices," *Nano-Micro Letters* 17 (2025): 197, https://doi.org/10.1007/s40820-024-01635-7.

19. A. Liu, X. Zhang, Z. Liu, et al., "The Roadmap of 2D Materials and Devices Toward Chips," *Nano-Micro Letters* 16 (2024): 119, https://doi.org/10.1007/s40820-023-01273-5.

20. J. Han, Z. Fu, J. Wei, et al., "2D Materials-Based Next-Generation Multidimensional Photodetectors," *Light: Science & Applications* 14 (2025): 362.

21. C. Liu, H. Chen, S. Wang, et al., "Two-dimensional materials for next-generation computing technologies," *Nature Nanotechnology* 15 (2020): 545, https://doi.org/10.1038/s41565-020-0724-3.

22. J. Zhang, Z. Hu, Q. Yang, et al., "Strong Anisotropy and Giant Photothermoelectricity of 1D Alloy Nb 3 Se 12 I-Based Photodetector for Ultrabroadband Light-Detection and Encryption Imaging Application," *Advanced Materials* 37 (2024): 2410275, https://doi.org/10.1002/adma.202410275.

23. M. Long, P. Wang, H. Fang, and W. Hu, "Progress, Challenges, and Opportunities for 2D Material Based Photodetectors," *Advanced Functional Materials* 29 (2018): 1803807, https://doi.org/10.1002/adfm.201803807.

24. Q. Qiu and Z. Huang, "Photodetectors of 2D Materials From Ultraviolet to Terahertz Waves," *Advanced Materials* 33 (2021): 2008126, https://doi.org/10.1002/adma.202008126.

25. H. Tian, Q. Guo, Y. Xie, et al., "Anisotropic Black Phosphorus Synaptic Device for Neuromorphic Applications," *Advanced Materials* 28 (2016): 4991–4997, https://doi.org/10.1002/adma.201600166.

26. Y. Yang, S. C. Liu, Y. Wang, et al., "In-Plane Optical Anisotropy of Low-Symmetry 2D GeSe," *Advanced Optical Materials* 7 (2018): 1801311, https://doi.org/10.1002/adom.201801311.

27. L. Li, P. Gong, D. Sheng, et al., "Highly In-Plane Anisotropic 2D GeAs 2 for Polarization-Sensitive Photodetection," *Advanced Materials* 30 (2018): 1804541, https://doi.org/10.1002/adma.201804541.

28. L. Li, W. Wang, P. Gong, et al., "2D GeP: An Unexploited Low-Symmetry Semiconductor With Strong In-Plane Anisotropy," *Advanced Materials* 30 (2018): 1706771, https://doi.org/10.1002/adma.201706771.

29. P. Li, J. Zhang, C. Zhu, et al., "Penta -PdPSe: A New 2D Pentagonal Material With Highly In-Plane Optical, Electronic, and Optoelectronic Anisotropy," *Advanced Materials* 33 (2021): 2102541, https://doi.org/10.1002/adma.202102541.

30. L. Pi, P. Wang, S.-J. Liang, et al., "Broadband Convolutional Processing using Band-Alignment-Tunable Heterostructures," *Nature Electronics* 5 (2022): 248–254, https://doi.org/10.1038/s41928-022-00747-5.

31. Y. Gong, R. Duan, Y. Hu, et al., "Reconfigurable and Nonvolatile Ferroelectric Bulk Photovoltaics based on 3R-WS2 for Machine Vision," *Nature Communications* 16 (2025): 230, https://doi.org/10.1038/s41467-024-55562-7.

32. L. Mennel, J. Symonowicz, S. Wachter, D. K. Polyushkin, A. J. Molina-Mendoza, and T. Mueller, "Ultrafast Machine Vision With 2D Material Neural Network Image Sensors," *Nature* 579 (2020): 62–66, https://doi.org/10.1038/s41586-020-2038-x.

33. Y. Yang, C. Pan, Y. Li, et al., "In-Sensor Dynamic Computing for Intelligent Machine Vision," *Nature Electronics* 7 (2024): 225–233, https://doi.org/10.1038/s41928-024-01124-0.

34. W. Fan, H. Yan, X. Wang, et al., "Polarization-Sensitive Photosynapse Based on PdSe 2 /WS 2 Heterostructure for Visible-Infrared Broadband Artificial Vision System," *Advanced Functional Materials* 35 (2025): 2416703, https://doi.org/10.1002/adfm.202416703.

35. L. Shan, C. Xu, J. Pan, et al., "A Simple Optical Convolution Strategy Based on Versatile Adjustable Optical Convolution Kernel for All-Optical Convolution Computing," *Advanced Materials* 37 (2025): 2420534, https://doi.org/10.1002/adma.202420534.

36. T. Li, J. Miao, X. Fu, et al., "Reconfigurable, Non-Volatile Neuromorphic Photovoltaics," *Nature Nanotechnology* 18 (2023): 1303–1310, https://doi.org/10.1038/s41565-023-01446-8.

37. L. Pi, C. Hu, W. Shen, et al., "Highly In-Plane Anisotropic 2D PdSe 2 for Polarized Photodetection With Orientation Selectivity," *Advanced Functional Materials* 31 (2021): 2006774, https://doi.org/10.1002/adfm.202006774.

38. F. Yang, K. Li, M. Fan, et al., "Strongly Anisotropic Quasi-1D BaTiS3 Chalcogenide Perovskite for Near-Infrared Polarized Photodetection," *Advanced Optical Materials* 11 (2022): 2201859.

39. R. Bai, T. Xiong, J. Zhou, et al., "Polarization-sensitive and wide-spectrum photovoltaic detector based on quasi-1D ZrGeTe4 nanoribbon," *InfoMat* 4 (2021): 12258.

40. J. Liu, H. Gan, Q. Hao, et al., "High-Performance Visible and Near-Infrared Dual-Band Photodetector based on Anisotropic 2D NbS3 with Perpendicularly Reversed Polarization Behaviors," *InfoMat* 7 (2024): 12625.

41. J. Han, W. Deng, F. Hu, et al., "2D Materials-Based Photodetectors With Bi-Directional Responses in Enabling Intelligent Optical Sensing," *Advanced Functional Materials* 35 (2025): 2423360, https://doi.org/10.1002/adfm.202423360.

42. J. Liao, H. Shao, Y. Zhang, et al., "Infrared In-Sensor Computing Based on Flexible Photothermoelectric Tellurium Nanomesh Arrays," *Advanced Materials* 37 (2025): 2419653, https://doi.org/10.1002/adma.202419653.

43. M. Dai, X. Zhang, and Q. J. Wang, "2D Materials for Photothermoelectric Detectors: Mechanisms, Materials, and Devices," *Advanced Functional Materials* 34 (2024): 2312872, https://doi.org/10.1002/adfm.202312872.

44. X. Lu, L. Sun, P. Jiang, and X. Bao, "Progress of Photodetectors Based on the Photothermoelectric Effect," *Advanced Materials* 31 (2019): 1902044, https://doi.org/10.1002/adma.201902044.

45. A. Mar and J. A. Ibers, "The Layered Ternary Germanium Tellurides ZrGeTe4, HfGeTe4, and TiGeTe6: Structure, Bonding, and Physical Properties," *Journal of the American Chemical Society* 115 (2002): 3227–3238, https://doi.org/10.1021/ja00061a022.

46. F. Wang, T. Zhang, R. Xie, Z. Wang, and W. Hu, "How to Characterize Figures of Merit of Two-Dimensional Photodetectors," *Nature Communications* 14 (2023): 2224, https://doi.org/10.1038/s41467-023-37635-1.

47. Y. Dang and X. Tao, "Recent Progress of Bulk Photovoltaic Effect in Acentric SINGLE Crystals and Optoelectronic Devices," *Matter* 5 (2022): 2659–2684.

48. D. Li, J.-K. Qin, B. Zhu, et al., "Intercorrelated Ferroelectricity and Bulk Photovoltaic Effect in Two-Dimensional Sn 2 P 2 S 6 Semiconductor for Polarization-Sensitive Photodetection," *ACS Nano* 18 (2024): 9636–9644, https://doi.org/10.1021/acsnano.4c00382.

49. Y. Li, J. Fu, X. Mao, et al., "Enhanced Bulk Photovoltaic Effect in Two-Dimensional Ferroelectric CuInP2S6," *Nature Communications* 12 (2021): 5896, https://doi.org/10.1038/s41467-021-26200-3.

50. M. Usman, S. Nisar, D.-K. Kim, et al., "Polarization-Sensitive Photodetection of Anisotropic 2D Black Arsenic," *The Journal of*

Physical Chemistry C 127 (2023): 9076–9082, https://doi.org/10.1021/acs.jpcc.2c08630.

51. Y. Fang, F. Wang, R. Wang, T. Zhai, and F. Huang, "2D NbOI 2: A Chiral Semiconductor With Highly In-Plane Anisotropic Electrical and Optical Properties," *Advanced Materials* 33 (2021): 2101505, https://doi.org/10.1002/adma.202101505.

52. R. Duan, Y. He, C. Zhu, et al., "2D Cairo Pentagonal PdPS: Air-Stable Anisotropic Ternary Semiconductor With High Optoelectronic Performance," *Advanced Functional Materials* 32 (2022): 2113255, https://doi.org/10.1002/adfm.202113255.

53. C. Sakaridis, D. Dai, and L. Gool, "ACDC: The Adverse Conditions Dataset with Correspondences for Semantic Driving Scene Understanding," *Proceedings of the IEEE/CVF international conference on computer vision* (2021): 10765–10775.

54. L. Chen, Y. Zhu, G. Papandreou, F. Schroff, and H. Adam, "Encoder-Decoder with Atrous Separable Convolution for Semantic Image Segmentation," *Proceedings of the European conference on computer vision (ECCV)* (2018): 801–818.

Supporting Information

Additional supporting information can be found online in the Supporting Information section.

Supporting File: adfm74245-sup-0001-SuppMat.docx.